Validation of the ECOSTRESS Land Surface Temperature Product Using Ground Measurements

Xiangchen Meng, *Associate Member, IEEE*, Jie Cheng, *Senior Member, IEEE*, Beibei Yao, and Yahui Guo

***Abstract*— The ECOsystem Spaceborne Thermal Radiometer Experiment on Space Station (ECOSTRESS) land surface temperature (LST) product provides LST data with a high-spatial resolution of 70 m × 70 m. In this letter, the quality of ECOSTRESS LST product was assessed using ground measurements collected from 17 sites, including seven surface radiation budget network (SURFRAD) sites, seven baseline surface radiation network (BSRN) sites, and three National Tibetan Plateau/Third Pole Environment Data Center (TPDC) sites. After outlier removal using the "3σ-Hampel identifier," the overall bias and root mean square error (RMSE) of ECOSTRESS LST at SURFRAD, BSRN, and TPDC sites are −1.61 and 3.08 K, −0.75, and 3.50 K, and −0.82 and 4.18 K, respectively. This letter shows the accuracy and uncertainty of ECOSTRESS LST product, and will benefit research fields that require LST with high-spatial resolution.**

***Index Terms*— Baseline surface radiation network (BSRN), ecosystem spaceborne thermal radiometer experiment on space station (ECOSTRESS), land surface temperature (LST), National Tibetan Plateau/Third Pole Environment Data Center (TPDC), surface radiation budget network (SURFRAD).**

I. Introduction

LAND surface temperature (LST) is a key parameter in land surface physical processes on regional and global scales [1]. LST is also an important input parameter for research on hydrology, urban climate, ecology, and so on [2]–[4]. Remote sensing is a unique way of obtaining the LST at regional and global scales. With the development of thermal infrared (TIR) remote sensing, several LST products, such as advanced spaceborne thermal emission and reflection radiometer (ASTER), moderate resolution imaging spectroradiometer (MODIS), visible infrared imager radiometer suite (VIIRS) [5], with different spatial and temporal resolutions have been generated and applied to drought monitoring, evapotranspiration, and climate change studies [6]–[8].

Manuscript received May 31, 2021; revised August 18, 2021 and October 12, 2021; accepted October 25, 2021. Date of publication October 27, 2021; date of current version January 11, 2022. This work was supported by the National Natural Science Foundation of China under Grant 42001363. *(Corresponding authors: Xiangchen Meng; Jie Cheng.)*

Xiangchen Meng is with the Rizhao Key Laboratory of Territory Spatial Planning and Ecological Construction and the School of Geography and Tourism, Qufu Normal University, Rizhao, Shandong 276826, China (e-mail: xiangchenmeng@yeah.net).

Jie Cheng is with the State Key Laboratory of Remote Sensing Science, Faculty of Geographical Science, Institute of Remote Sensing Science and Engineering, Beijing Normal University, Beijing 100875, China (e-mail: jie_cheng@bnu.edu.cn).

Beibei Yao is with the School of Marxism, Qufu Normal University, Rizhao, Shandong 276826, China (e-mail: beibeiyao@qfnu.edu.cn).

Yahui Guo is with the College of Water Sciences, Beijing Normal University, Beijing 100875, China (e-mail: guoyh@mail.bnu.edu.cn).

Digital Object Identifier 10.1109/LGRS.2021.3123816

The ECOsystem Spaceborne Thermal Radiometer Experiment on Space Station (ECOSTRESS) was launched to the International Space Station (ISS) on June 29, 2018 [9]. ECOSTRESS TIR images are captured in five spectral channels centered on 8.29, 8.78, 9.20, 10.49, and 12.09 μm, with a high-spatial resolution (38 m × 69 m pixels) and revisit time (about three–five days) [10]. The ECOSTRESS LST product, which generated using the temperature emissivity separation (TES) algorithm [11], [12] is publicly available to the user community since July 9, 2018. With a high-spatial resolution of 70 m × 70 m, the ECOSTRESS LST product has significant potential for exploring plant water use and stress, agricultural water management, urban heat island, and volcanology studies.

The released LST products, e.g., MODIS, VIIRS, and Landsat LST, have been validated by researchers using temperature-based (T-based) method and radiance-based (R-based) method [13]–[16]. At present, although ground measurements have been used to validate the ECOSTRESS LST product [17], [18], the exploration about the validation of ECOSTRESS LST is still insufficient. Assessing the accuracy of ECOSTRESS LST products will help encourage the use across a wide range of applications. This study aims to validate the ECOSTRESS LST product with T-based method using ground measurements. This letter is organized as follows: Section II introduces the used satellite data, ground measurements, and the validation metrics. Section III provides the validation results and discussion. Section IV shows the conclusions of this study.

II. Data and Preprocessing

A. ECOSTRESS Level 2 Product

ECOSTRESS level-2 LST and emissivity (LST&E) product was downloaded from https://search.earthdata.nasa.gov. A physics-based TES algorithm is used for simultaneously retrieving the LST&E from ECOSTRESS level-1 data. The LST&E product contains 15 scientific datasets (SDSs), including the LST, LST error, land surface emissivity (LSE) and LSE error for the five spectral bands, broadband emissivity, precipitable water vapor, and quality control (QC) for LST&E.

A pair of *in situ* LST and ECOSTRESS LST can be obtained after the spatial–temporal match and QC. First, the nearest neighbor sampling method is used to obtain the spatial matching data based on the longitude and latitude of the validation site. Second, two *in situ* LSTs closest to ECOSTRESS overpass time are linearly interpolated to obtain the temporal matching data. Finally, LSTs with the best quality and nominal quality are selected as the final matchup according to the QC band of ECOSTRESS LST&E product. In total, we obtained

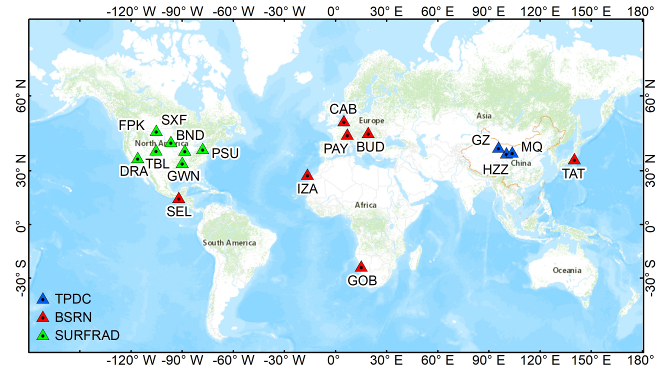

Fig. 1. Distribution of the *in situ* sites.

more than 3000 ECOSTRESS LST images between August 1, 2018 and December 31, 2020. After the spatial–temporal match and QC, only 753, 401, and 110 matchups were obtained at surface radiation budget network (SURFRAD), baseline surface radiation network (BSRN), and National Tibetan Plateau/Third Pole Environment Data Center (TPDC) sites, respectively.

B. LST Validation Sites

Ground measurements come from SURFRAD, BSRN, and TPDC are used to validate the accuracy of ECOSTRESS LST. The tower-based instrument pyranometer measures high-quality upwelling and downwelling shortwave and longwave radiation via Eppley [precision infrared pyrgeometers (PIR)], EKO (MR-60), Kipp and Zonen (CG4/CGR3/CGR4/CNR1/CNR4), which have been widely used to validate LST products and surface longwave radiation products [15], [19]–[27]. In this study, ground measurements collected from seven SURFRAD sites, seven BSRN sites, and three TPDC sites were used to validate the accuracy of ECOSTRESS LST, which can be downloaded from the following website: https://gml.noaa.gov/grad/field.html, https://bsrn.awi.de/, and https://data.tpdc.ac.cn/, respectively.

Due to the cosine response of the pyranometer, the downward facing pyranometer has 81° effective field of view [28]. Based on the tower height, the diameter of ground measurements footprint in the horizontal plane for each site is listed in Table I. Besides, the site distribution and specific information of each *in situ* site are also shown in Fig. 1 and Table I.

In situ LSTs can be converted by upwelling and downwelling longwave radiations observation using Stefan–Boltzmann law

$$T_s = \left[\frac{F^{\uparrow} - (1-\varepsilon_b)F^{\downarrow}}{\varepsilon_b \sigma}\right]^{\frac{1}{4}} \tag{1}$$

where T_s is ground LST, $F^{\uparrow}$ is the measured upwelling longwave radiation, $F^{\downarrow}$ is the measured downwelling longwave radiation, σ is the Stefan–Boltzmann's constant (5.67×10^{-8} W/m^2/K^4), ε_b is the broadband emissivity, which can be calculated from *in situ* emissivity or the five ASTER narrowband emissivity using the following equation [19]:

$$\begin{aligned}\varepsilon_b = {} & 0.197 + 0.025\varepsilon_{10} + 0.057\varepsilon_{11} \\ & + 0.237\varepsilon_{12} + 0.333\varepsilon_{13} + 0.146\varepsilon_{14}.\end{aligned} \tag{2}$$

TABLE I

SPECIFIC INFORMATION FOR EACH SITE

	Site	Lat	Lon	Surface type	Tower height	Footprint
SURFRAD	BND	40.052	-88.373	cropland		
	GWN	34.255	-89.873	grassland		
	PSU	40.720	-77.931	cropland		
	SXF	43.734	-96.623	grassland		
	FPK	48.308	-105.102	grassland	10m	~126m
	TBL	40.126	-105.238	grassland		
	DRA	36.623	-116.020	shrubland		
BSRN	BUD	47.429	19.182	grassland		
	CAB	51.971	4.927	grassland		
	GOB	-23.561	15.042	desert	2m	~25m
	IZA	28.309	-16.499	rock		
	PAY	46.815	6.944	cropland		
	SEL	15.784	-91.990	grassland		
	TAT	36.058	140.126	grassland		
TPDC	GZ	41.405	95.673	desert	4m	~50m
	HZZ	38.766	100.320	desert	6m	~76m
	MQ	39.208	103.668	desert	4m	~50m

C. Validation Metrics

For the LST matchups, average ECOSTRESS LSTs of 1 × 1 pixel and 3 × 3 pixels were extracted from the standard ECO2LSTE product. The performance of the ECOSTRESS LST product was assessed through two error metrics: the average difference (Bias) and the root mean square error (RMSE). To minimize the impact of cloud contamination and the uncertainty of ground measurements, the "3σ-Hampel identifier" [21], [29] is used to filter outliers that existed in the LST matchups. In this letter, the differences between ECOSTRESS and *in situ* LST were calculated, and then LST matchups with LST differences less than median-3S or larger than median+3S are regarded as outliers [21]. The S is described as

$$S = 1.4826 * \text{median}\{|x_i - x_m|\} \tag{3}$$

where x_i is the data sequence of the differences between ECOSTRESS and *in situ* LST, and x_m the median value of the x_i.

III. RESULTS AND DISCUSSION

A. Validation Result Before Outlier Removal

The validation results of ECOSTRESS LST before outlier removal are shown in Table II. As shown in Table II, the accuracy for the 1 × 1 pixel and 3 × 3 pixels is similar, the bias is between −1.9 and 1.7 K for most *in situ* sites, and larger than 2.0 K for GoodwinCreek (GWN), Desert Rock (DRA), Budapest (BUD), and HuaZhaiZi (HZZ) sites. Most of the RMSEs are larger than 3.0 K, whereas at BUD, Cabauw (CAB), Sioux Falls (SXF), Fort Peck (FPK), HZZ, and MinQin (MQ) sites are larger than 7.0 K.

To analyze the reasons for large biases at the BUD, CAB, FPK, SXF, HZZ, and MQ sites, the line charts between ECOSTRESS LST and *in situ* LST for all matchups at those sites are shown in Fig. 2. As shown in Fig. 2, there are clearly some extreme outliers in the ECOSTRESS LST and *in situ* LST, e.g., the ECOSTRESS LST is higher than 400 K at FPK site, the *in situ* LST is nearly 250 K at SXF site. To explain

TABLE II

VALIDATION RESULT OF ECOSTRESS LST PRODUCT FOR EACH SITE BEFORE OUTLIER REMOVAL

Site	Num.	1×1 pixel		3×3 pixel	
		Bias(K)	RMSE (K)	Bias (K)	RMSE (K)
BND	92	-1.34	4.76	-1.36	4.02
GWN	66	-2.05	4.25	-1.88	4.43
PSU	45	-0.7	2.68	-0.64	2.66
SXF	96	-0.02	7.73	0.09	7.51
FPK	145	0.96	14.9	1.14	12.58
TBL	134	-0.88	4.59	-1.30	4.48
DRA	175	-3.86	4.38	-3.87	4.38
BUD	73	-2.75	7.00	-3.12	7.24
CAB	104	-0.63	8.28	-0.65	8.34
GOB	116	0.94	3.42	0.69	3.22
IZA	24	-1.24	3.98	0.08	3.48
PAY	45	1.54	4.05	1.43	3.92
SEL	19	-0.77	2.74	-1.06	2.40
TAT	20	-0.92	3.80	-0. 94	3.91
GZ	56	-0.77	5.82	-0.82	5.81
HZZ	38	4.82	10.74	4.83	10.82
MQ	16	1.55	8.89	1.66	8.92

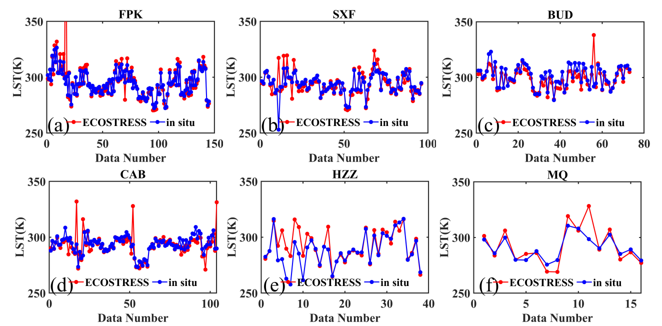

Fig. 2. Plots of ECOSTRESS LSTs and *in situ* LSTs at the (a) FPK, (b) SXF, (c) BUD, (d) CAB, (e) HZZ, and (f) MQ sites.

the reason more intuitively for larger bias, sample images of ECOSTRESS LST at the BUD, CAB, FPK, SXF, HZZ, and MQ sites are shown in Fig. 3. Obviously, the overestimated LST at FPK, BUD, CAB, and MQ sites is due to the noticeable strips. Based on the analysis of time series graphs and images of adjacent dates, the underestimated LST at the FPK, SXF, CAB, and MQ sites is due to the unmasked cloud pixels. As for the HZZ site, part of the overestimated LST is due to the noticeable strips and the other is the underestimation of ground observations (the LST is close to 260 K during the daytime of summer). Besides, the overestimated LST at SXF sites may be due to the inaccurate LSE estimation (<0.94), which is affected by the surrounding cloud.

In total, the outliers may be explained by three possible reasons. First, accurate cloud identification is a challenging endeavor, cloudy pixels in the ECOSTRESS LST product cannot be completely masked, primarily due to the limitations of having only calibrated ECOSTRESS thermal bands available for the cloud mask detection algorithm. Second, according to the statistics of ECOSTRESS LSE at the BUD, CAB, and SXF sites, part of ECOSTRESS LSE for channel 4 (10.49 μm) is less than 0.80, which may be unreasonable for grassland. On the one hand, the error of the TES algorithm will bring uncertainty to the LSE product. On the other hand, the undetected clouds also influence the accuracy of the retrieved LSE. Third, measurement error or noise exists in ground observations might increase the uncertainty of ground truth [30].

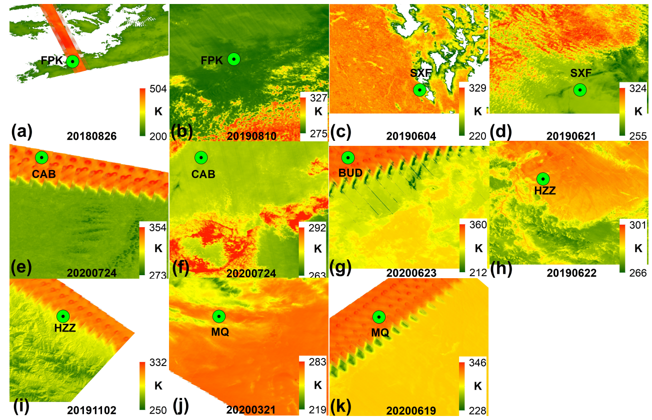

Fig. 3. Sample images of ECOSTRESS LST at the (a) and (b) FPK, (c) and (d) SXF, (e) and (f) CAB, (g) BUD, (h) and (i) HZZ, and (j) and (k) MQ sites.

TABLE III

VALIDATION RESULT OF ECOSTRESS LST PRODUCT FOR EACH SITE AFTER OUTLIER REMOVAL

Site	1×1 pixel			3×3 pixel		
	Num.	Bias(K)	RMSE(K)	Num.	Bias(K)	RMSE(K)
BND	81	-1.31	2.53	80	-1.49	2.35
GWN	60	-1.44	2.14	60	-1.41	1.97
PSU	41	-0.66	1.35	41	-0.59	1.41
SXF	79	-1.19	1.98	86	-0.66	2.09
FPK	137	-0.33	2.13	136	-0.04	2.33
TBL	125	-0.88	3.61	121	-1.43	3.31
DRA	173	-3.79	4.27	173	-3.80	4.28
BUD	72	-3.43	4.47	72	-3.81	4.88
CAB	93	-1.42	2.61	92	-1.43	2.45
GOB	115	0.86	3.29	115	0.60	3.07
IZA	22	-2.06	3.38	24	0.08	3.48
PAY	45	1.54	4.05	45	1.43	3.92
SEL	19	-0.77	2.74	19	-1.06	2.40
TAT	20	-0.92	3.80	20	-0. 94	3.91
GZ	55	-1.27	4.64	55	-1.33	4.59
HZZ	29	-0.22	2.40	29	-0.27	2.37
MQ	15	-0.33	5.02	15	-0.22	5.04

B. Validation Result After Outlier Removal

The bias and RMSE of the differences between ECOSTRESS LST and *in situ* LST after removing the outlier for each site are shown in Table III. After the outlier removal, the accuracy is also similar for the 1 × 1 pixel and 3 × 3 pixels results, but the number of effective LST matchups for some sites is different. For 1 × 1 pixel result, the bias ranges from −3.79 to −0.33 K at SURFRAD sites, whereas RMSE ranges from 1.35 to 4.27 K. The accuracy and uncertainty of ECOSTRESS LST product at BSRN sites is worse than that at SURFRAD sites, with bias (RMSE) ranges from −3.43 K (2.61 K) to 1.54 K (4.47 K). As for TPDC sites, the bias ranges from −1.27 to −0.22 K, whereas RMSE ranges from 2.40 to 5.02 K. For 3 × 3 pixels result, the bias (RMSE) ranges from −3.80 K (1.41 K) to −0.04 K (4.28 K), −3.81 K (2.40 K) to 1.43 K (4.88 K), and −1.33 K (2.37 K) to −0.22 K (5.04 K) for SURFRAD, BSRN, and TPDC sites, respectively.

Fig. 4 shows the scatterplots between ECOSTRESS LST and *in situ* LST at SURFRAD, BSRN, TPDC, and all sites after removing the outlier. The overall biases and RMSEs are also similar for the 1 × 1 pixel and 3 × 3 pixels results, with biases (RMSEs) between −0.75 K (3.02 K) and −1.61 K (4.18 K). It is worth noting that the bias at SURFRAD

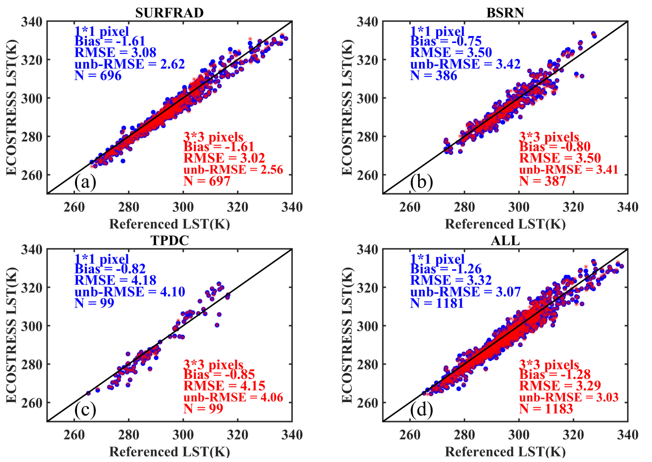

Fig. 4. Scatterplots between ECOSTRESS LSTs and *in situ* LSTs at the (a) SURFRAD, (b) BSRN, (c) TPDC, and (d) all sites after removing the outlier.

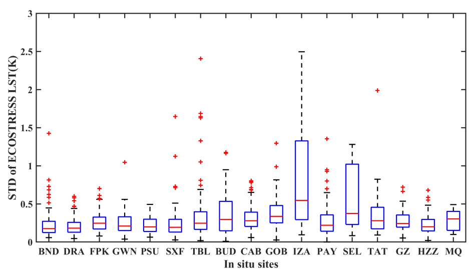

Fig. 5. Boxplots of the STD of ECOSTRESS LST (statistics of a window of 3 × 3 pixels) for each site.

sites is larger than that of BSRN sites, but the RMSE is the opposite. When the evaluation results based on the bias and RMSE are inconsistent, the unbiased RMSE defined as $(\text{RMSE}^2 - \text{bias}^2)^{1/2}$ by Vanhellemont [31] may be considered as an indicator of the total error. As shown in Fig. 4, the unbiased RMSEs at SURFRAD, BSRN, TPDC, and all sites are 2.62 K (2.56 K), 3.42 K (3.41 K), 4.10 K (4.06 K), and 3.07 K (3.03 K), respectively, for 1 × 1 pixel (3 × 3 pixels) results. Hulley *et al.* [18] evaluated the accuracy of ECOSTRESS LST using the T-based and R-based methods, with an average RMSE (mean absolute error) of 1.07 K (0.40 K) at all sites. For the T-based method, ground measurements collected from three Jet Propulsion Laboratory (JPL) sites and two Karlsruhe Institute of Technology (KIT) sites were used to validate LST. About 83% of the LST matchups are acquired at inland water sites, with more homogeneous in spatial and temporal scale. In this study, LST matchups are acquired on 17 sites covered by vegetation and desert, which can supplement the current validation work.

As the spatial representation of the site has an important impact on validation, the standard deviation (STD) of ECOSTRESS LST for the 3 × 3 pixels was also calculated as an estimate of the spatial heterogeneity of the *in situ* sites. Fig. 5 shows boxplots of the STD of ECOSTRESS LST for each site. The STD of LST at SURFRAD and TPDC sites is less than 0.5 K for most cases, which indicated the SURFRAD and TPDC sites are more homogeneous than BSRN sites at the ECOSTRESS pixel scale. Although the Izana (IZA) and Selegua (SEL) sites seem more heterogeneous than other sites at the ECOSTRESS pixel scale, the bias and RMSE at these sites did not significantly increase. This phenomenon can be explained by the following reasons.

1) ECOSTRESS LST product was validated with the limited matchup and the validation results may vary depending on the number of the valid matchups.
2) Theoretically, ground observations on BSRN sites with small time intervals (1 min) are closer to the ECOSTRESS LST because LST changes rapidly with time.

C. Discussion

Although, robust outlier existed in the LST matchups were removed before validation, negative biases, and large uncertainty (>3.0 K) were found. Possible reasons for large uncertainty are the inaccurate cloud detection, the heterogeneity of *in situ* sites, and the uncertainty of algorithm. First, as mentioned in Section III, cloudy pixels in the ECOSTRESS LST product cannot be completely masked, which may bring uncertainty to LST product. Second, ideally validation of LST product requires a site that is homogeneous in temperature at the scale of the imagery. Although the heterogeneity of SURFRAD sites have been widely discussed [13], [32], the spatial and temporal representativeness of BSRN and TPDC sites is still unresolved and needs to be evaluated before LST validation. Moreover, as indicated by Malakar *et al.* [15], spatial heterogeneity of LST at the DRA and TableMountain (TBL) sites is larger than that of other SURFRAD sites, which need to be excluded for the validation of LST products with high-spatial resolution. Except for the DRA and TBL sites, the bias (RMSE) of ECOSTRESS LST product ranges from −1.44 K (1.35 K) to −0.33 K (2.53 K) at SURFRAD sites. Finally, as point out in the algorithm theoretical basis documents (ATBDs) of level 2 product, due to the mass storage unit failure anomalies, level 2 product generated using the original five-band TES algorithm was changed to use the three-band TES algorithm after May 15, 2019, with RMSE increase from approximately 1 to near 1.5 K based on simulations. In addition, the tower-based measurements usually cannot represent satellite sensor footprint, up-scaling model may be used to estimate the uncertainty of LST product [13]. Furthermore, as a supplement of T-based method, the R-based method does not require *in situ* LSTs, we can collect atmospheric profiles at the time of satellite overpass and the surface emissivity to validate LST products at the global scale.

IV. Conclusion

In this study, the accuracy and uncertainty of ECOSTRESS LST products, which acquired over 2 years from August 1, 2018 and December 31, 2020, was validated using T-based method by ground measurements collected from 17 sites, including seven SURFRAD sites, seven BSRN sites, and three TPDC sites. Considering the accurate cloud identification is a challenging endeavor, outliers existed in the LST matchups were filtered using the "3σ-Hampel identifier." According to the analysis, the outliers are mainly caused by the noticeable strips, the unmasked cloud pixels, and the uncertainty of ground observations. The validation results indicate that the ECOSTRESS LST product underestimates the LSTs. For the 1 × 1 pixel results, the biases (RMSEs) of SURFRAD, BSRN, and TPDC sites are −1.61 K (3.08 K), −0.75 K (3.50 K), and −0.82 K (4.18 K), respectively. As for the 3 × 3 pixels results, those values are −1.61 K (3.02 K), −0.80 K (3.50 K), and −0.85 K (4.15 K), respectively. The overall bias, RMSE, and unbiased RMSE of all sites is −1.26 K (−1.28 K), 3.32 K (3.29 K), and 3.07 K (3.03 K) for the 1 × 1 pixel (3 × 3 pixels) results. The validation of ECOSTRESS LST products using ground measurements will facilitate the use of the LST product for drought monitoring, evapotranspiration, and climate change studies.

References

[1] Z. Wan and J. Dozier, "A generalized split-window algorithm for retrieving land-surface temperature from space," *IEEE Trans. Geosci. Remote Sens.*, vol. 34, no. 4, pp. 892–905, Jul. 1996.

[2] M. C. Anderson, J. M. Norman, W. P. Kustas, R. Houborg, P. J. Starks, and N. Agam, "A thermal-based remote sensing technique for routine mapping of land-surface carbon, water and energy fluxes from field to regional scales," *Remote Sens. Environ.*, vol. 112, no. 12, pp. 4227–4241, Dec. 2008, doi: 10.1016/j.rse.2008.07.009.

[3] S.-B. Duan, Z.-L. Li, B.-H. Tang, H. Wu, and R. Tang, "Generation of a time-consistent land surface temperature product from MODIS data," *Remote Sens. Environ.*, vol. 140, pp. 339–349, Jan. 2014, doi: 10.1016/j.rse.2013.09.003.

[4] J. A. Sobrino, F. Del Frate, M. Drusch, J. C. Jiménez-Muñoz, P. Manunta, and A. Regan, "Review of thermal infrared applications and requirements for future high-resolution sensors," *IEEE Trans. Geosci. Remote Sens.*, vol. 54, no. 5, pp. 2963–2972, May 2016, doi: 10.1109/TGRS.2015.2509179.

[5] H. Li *et al.*, "Evaluation of atmospheric correction methods for the ASTER temperature and emissivity separation algorithm using ground observation networks in the HiWATER experiment," *IEEE Trans. Geosci. Remote Sens.*, vol. 57, no. 5, pp. 3001–3014, May 2019, doi: 10.1109/TGRS.2018.2879316.

[6] J. Hansen, R. Ruedy, M. Sato, and K. Lo, "Global surface temperature change," *Rev. Geophys.*, vol. 48, no. 4, 2010, doi: 10.1029/2010rg000345.

[7] J. Cheng and W. Kustas, "Using very high resolution thermal infrared imagery for more accurate determination of the impact of land cover differences on evapotranspiration in an irrigated agricultural area," *Remote Sens.*, vol. 11, no. 6, p. 613, Mar. 2019, doi: 10.3390/rs11060613.

[8] T. Hu *et al.*, "Monitoring agricultural drought in Australia using MTSAT-2 land surface temperature retrievals," *Remote Sens. Environ.*, vol. 236, Jan. 2020, Art. no. 111419, doi: 10.1016/j.rse.2019.111419.

[9] S. J. Hook *et al.*, "In-flight validation of the ECOSTRESS, Landsats 7 and 8 thermal infrared spectral channels using the Lake Tahoe CA/NV and Salton Sea CA automated validation sites," *IEEE Trans. Geosci. Remote Sens.*, vol. 58, no. 2, pp. 1294–1302, Feb. 2020, doi: 10.1109/TGRS.2019.2945701.

[10] G. Hulley, S. Shivers, E. Wetherley, and R. Cudd, "New ECOSTRESS and MODIS land surface temperature data reveal fine-scale heat vulnerability in cities: A case study for Los Angeles County, California," *Remote Sens.*, vol. 11, no. 18, p. 2136, Sep. 2019, doi: 10.3390/rs11182136.

[11] A. Gillespie *et al.*, "A temperature and emissivity separation algorithm for Advanced Spaceborne Thermal Emission and Reflection Radiometer (ASTER) images," *IEEE Trans. Geosci. Remote Sens.*, vol. 36, no. 4, pp. 1113–1126, Apr. 1998.

[12] T. Islam, G. C. Hulley, N. K. Malakar, R. G. Radocinski, P. C. Guillevic, and S. J. Hook, "A physics-based algorithm for the simultaneous retrieval of land surface temperature and emissivity from VIIRS thermal infrared data," *IEEE Trans. Geosci. Remote Sens.*, vol. 55, no. 1, pp. 563–576, Jan. 2017, doi: 10.1109/TGRS.2016.2611566.

[13] P. C. Guillevic *et al.*, "Land surface temperature product validation using NOAA's surface climate observation networks—Scaling methodology for the Visible Infrared Imager Radiometer Suite (VIIRS)," *Remote Sens. Environ.*, vol. 124, pp. 282–298, Sep. 2012, doi: 10.1016/j.rse.2012.05.004.

[14] S.-B. Duan, Z.-L. Li, H. Wu, P. Leng, M. Gao, and C. Wang, "Radiance-based validation of land surface tesmperature products derived from collection 6 MODIS thermal infrared data," *Int. J. Appl. Earth Observ. Geoinf.*, vol. 70, pp. 84–92, Aug. 2018, doi: 10.1016/j.jag.2018.04.006.

[15] N. K. Malakar, G. C. Hulley, S. J. Hook, K. Laraby, M. Cook, and J. R. Schott, "An operational land surface temperature product for Landsat thermal data: Methodology and validation," *IEEE Trans. Geosci. Remote Sens.*, vol. 56, no. 10, pp. 5717–5735, Oct. 2018, doi: 10.1109/TGRS.2018.2824828.

[16] H. Li *et al.*, "Temperature-based and radiance-based validation of the collection 6 MYD11 and MYD21 land surface temperature products over barren surfaces in Northwestern China," *IEEE Trans. Geosci. Remote Sens.*, vol. 59, no. 2, pp. 1–14, Feb. 2020, doi: 10.1109/TGRS.2020.2998945.

[17] N. Liu, A. C. Oishi, C. F. Miniat, and P. Bolstad, "An evaluation of ECOSTRESS products of a temperate montane humid forest in a complex terrain environment," *Remote Sens. Environ.*, vol. 265, Nov. 2021, Art. no. 112662, doi: 10.1016/j.rse.2021.112662.

[18] G. C. Hulley *et al.*, "Validation and quality assessment of the ECOSTRESS level-2 land surface temperature and emissivity product," *IEEE Trans. Geosci. Remote Sens.*, early access, Jun. 4, 2021, doi: 10.1109/TGRS.2021.3079879.

[19] J. Cheng, S. Liang, Y. Yao, and X. Zhang, "Estimating the optimal broadband emissivity spectral range for calculating surface longwave net radiation," *IEEE Geosci. Remote Sens. Lett.*, vol. 10, no. 2, pp. 401–405, Mar. 2013, doi: 10.1109/LGRS.2012.2206367.

[20] P. C. Guillevic *et al.*, "Validation of land surface temperature products derived from the Visible Infrared Imaging Radiometer Suite (VIIRS) using ground-based and heritage satellite measurements," (in English), *Remote Sens. Environ.*, vol. 154, pp. 19–37, Nov. 2014, doi: 10.1016/j.rse.2014.08.013.

[21] S.-B. Duan *et al.*, "Validation of collection 6 MODIS land surface temperature product using *in situ* measurements," *Remote Sens. Environ.*, vol. 225, pp. 16–29, May 2019, doi: 10.1016/j.rse.2019.02.020.

[22] X. Meng, J. Cheng, S. Zhao, S. Liu, and Y. Yao, "Estimating land surface temperature from Landsat-8 data using the NOAA JPSS enterprise algorithm," *Remote Sens.*, vol. 11, p. 155, Jan. 2019, doi: 10.3390/rs11020155.

[23] H. Wang, Y. Yu, P. Yu, and Y. Liu, "Land surface emissivity product for NOAA JPSS and GOES-R missions: Methodology and evaluation," *IEEE Trans. Geosci. Remote Sens.*, vol. 58, no. 1, pp. 307–318, Jan. 2020, doi: 10.1109/tgrs.2019.2936297.

[24] Q. Zeng, J. Cheng, and L. Dong, "Assessment of the long-term high-spatial-resolution global land surface satellite (GLASS) surface longwave radiation product using ground measurements," *IEEE J. Sel. Topics Appl. Earth Observ. Remote Sens.*, vol. 13, pp. 2032–2055, 2020, doi: 10.1109/JSTARS.2020.2992472.

[25] S. L. Ermida, P. Soares, V. Mantas, F.-M. Göttsche, and I. F. Trigo, "Google Earth engine open-source code for land surface temperature estimation from the Landsat series," *Remote Sens.*, vol. 12, no. 9, p. 1471, May 2020, doi: 10.3390/rs12091471.

[26] M. Wang *et al.*, "An efficient framework for producing Landsat-based land surface temperature data using Google Earth engine," *IEEE J. Sel. Topics Appl. Earth Observ. Remote Sens.*, vol. 13, pp. 4689–4701, 2020, doi: 10.1109/jstars.2020.3014586.

[27] S. Zhou and J. Cheng, "An improved temperature and emissivity separation algorithm for the advanced Himawari imager," *IEEE Trans. Geosci. Remote Sens.*, vol. 58, no. 10, pp. 7105–7124, Oct. 2020, doi: 10.1109/TGRS.2020.2979846.

[28] Y. Shuai, J. G. Masek, F. Gao, and C. B. Schaaf, "An algorithm for the retrieval of 30-m snow-free albedo from Landsat surface reflectance and MODIS BRDF," *Remote Sens. Environ.*, vol. 115, no. 9, pp. 2204–2216, 2011, doi: 10.1016/j.rse.2011.04.019.

[29] F.-M. Göttsche, F.-S. Olesen, and A. Bork-Unkelbach, "Validation of land surface temperature derived from MSG/SEVIRI with *in situ* measurements at Gobabeb, Namibia," *Int. J. Remote Sens.*, vol. 34, nos. 9–10, pp. 3069–3083, May 2013, doi: 10.1080/01431161.2012.716539.

[30] S. Li, Y. Yu, D. Sun, D. Tarpley, X. Zhan, and L. Chiu, "Evaluation of 10 year AQUA/MODIS land surface temperature with SURFRAD observations," (in English), *Int. J. Remote Sens.*, vol. 35, no. 3, pp. 830–856, Feb. 2014, doi: 10.1080/01431161.2013.873149.

[31] Q. Vanhellemont, "Combined land surface emissivity and temperature estimation from landsat 8 OLI and TIRS," *ISPRS J. Photogramm. Remote Sens.*, vol. 166, pp. 390–402, Aug. 2020, doi: 10.1016/j.isprsjprs.2020.06.007.

[32] K. Wang and S. Liang, "Evaluation of ASTER and MODIS land surface temperature and emissivity products using long-term surface longwave radiation observations at SURFRAD sites," *Remote Sens. Environ.*, vol. 113, no. 7, pp. 1556–1565, 2009, doi: 10.1016/j.rse.2009.03.009.